DONALD R. THOMPSON

INTENSITY MODULATIONS IN SYNTHETIC APERTURE RADAR IMAGES OF OCEAN SURFACE CURRENTS AND THE WAVE/CURRENT INTERACTION PROCESS

The physics that determines the perturbation of the ocean surface-wave spectrum due to the presence of a slowly varying surface current is examined. In the limit of Bragg scattering, this perturbation is related to the intensity modulation in radar backscatter from the ocean surface. Using ground-truth data obtained from recent experiments as input, we compute the expected modulation at L and X band and compare the results with the observed modulation from concurrent synthetic aperture radar images. At L band, the comparison is found to show good agreement; at X band, a more complicated two-step mechanism must be invoked.

INTRODUCTION

During the past decade or so, rapid advances in the field of remote sensing have enabled us to examine many interesting properties of the ocean surface. In particular, the development of synthetic aperture radar (SAR) has provided an extensive and rich database for studying a wide variety of oceanographic phenomena, an excellent description of which is given in Ref. 1, along with images showing such mesoscale features as major current boundaries, warm and cold water eddies associated with the Gulf Stream, and surface manifestations of the bathymetry.

Because of the large number of uncontrollable and unmeasured parameters during a SAR overflight, it is usually not possible to determine which of many possible mechanisms is responsible for producing the features that are visible on the SAR images. Recently, however, APL has been involved in experiments designed to obtain relevant ground-truth data concurrently with the SAR overflight in order to understand some of the possible imaging mechanisms. In particular, the SAR Signature Experiment (SARSEX) (which is described in the article by Gasparovic et al. elsewhere in this issue) is concerned with understanding the SAR imaging mechanism for internal waves.

In Fig. 1, we show X-band ($f_R = 9.35 \times 10^9$ hertz) and L-band ($f_R = 1.25 \times 10^9$ hertz) SAR images of internal waves taken in the late summer of 1984 in the New York Bight area off the eastern United States coast. The waves are generated by tidal flow over the continental shelf break about 150 kilometers southeast of Long Island. The research vessels that collected ground-truth data can be seen as bright spots near the bottom of the images. Since the 10^9 hertz microwave radiation from the SAR penetrates only a few centimeters into seawater, it is clear that the bright and dark streaks in these images are caused by some surface manifestation of internal waves. Furthermore, the mean surface displacement arising from the passage of the internal wave is much too small to be resolved by the SAR. It is, in fact, the horizontal surface velocity field of the internal wave interacting with the surface waves that is responsible for the SAR backscatter modulation seen in Fig. 1. This interaction results in a modulation in the surface-wave displacement spectrum. Because the SAR is sensitive to surface roughness on scales of the order of the radar wavelength, modulations of the surface spectrum at these scales by the internal wave surface currents produce the intensity modulations seen on the SAR images.

It is the purpose of this article to develop a more precise description of the wave/current interaction process. In the next section, it will be shown how the degree of modulation in the wave-height spectrum of the surface waves is related to the properties of the surface current field; how this modulation is related to the observed intensity modulations in the SAR image will also be discussed. Finally, we will return to our discussion of Fig. 1 and attempt to describe quantitatively the magnitude of the observed modulations on the basis of our understanding of the wave/current interaction process.

WAVE/CURRENT INTERACTION THEORY

Wave/current interaction theory has been discussed in many books and articles over the past years. One should see, for example, Refs. 2 through 6 and the references contained therein for a thorough treatment of the problem. We present here a brief development based on the geometrical techniques of ray theory and the stationary phase approximation, which is an asymptotic representation of dispersive wave fields.
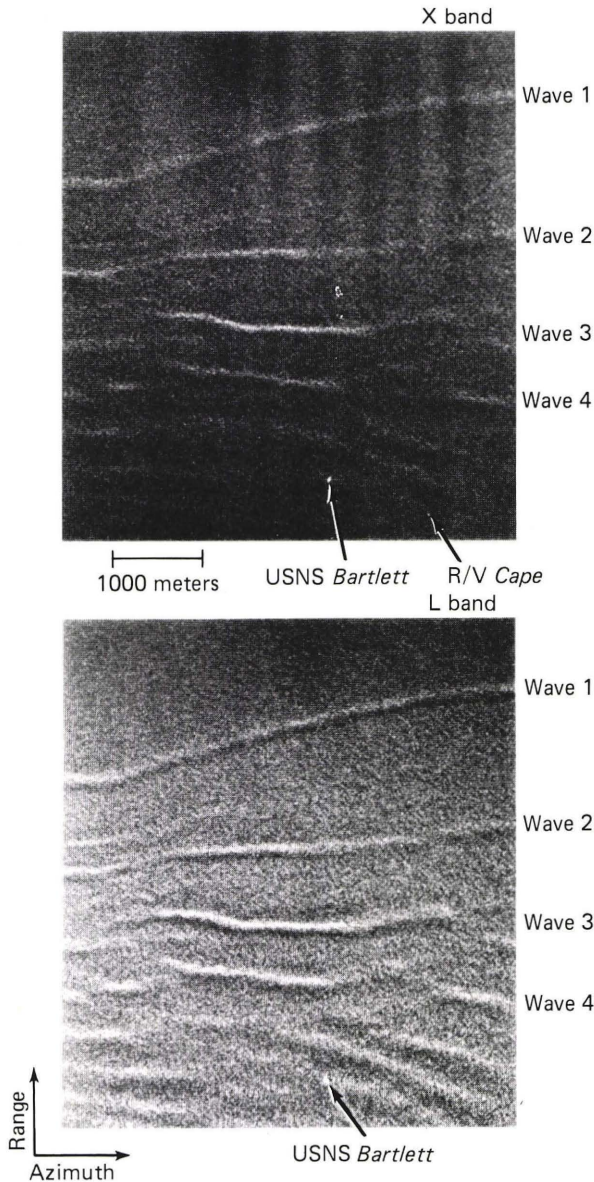
Figure 1—Concurrent X- and L-band SAR images of internal waves recorded during the SARSEX.

A general description of a linear dispersive wave field, $\xi(\mathbf{x},t)$, can be written as

$$\xi(\mathbf{x},t) = \int G(\mathbf{k}) \exp \{i\mathbf{k} \cdot \mathbf{x} - \omega(\mathbf{k})t\} \, d\mathbf{k} , \quad (1)$$

where

$$G(\mathbf{k}) = (2\pi)^{-2} \int \xi(\mathbf{x},0) \exp \{-i\mathbf{k} \cdot \mathbf{x}\} \, d\mathbf{x} , \quad (2)$$

and $\omega(\mathbf{k})$ is the dispersion relation between ω and $\mathbf{k}$. In the limit of large $\mathbf{x}$ and t, Eq. 1 may be solved approximately by recognizing that for slowly varying $G(\mathbf{k})$, the main contribution to the integral comes from the region in $\mathbf{k}$ space that satisfies

$$\nabla_\mathbf{k} [\mathbf{k} \cdot \mathbf{x} - \omega(\mathbf{k})t] = 0. \quad (3)$$

The $\mathbf{k}$ value that satisfies Eq. 3, $\mathbf{k}_s = \mathbf{k}_s(\mathbf{x},t)$, defines the point of stationary phase. For slowly varying $G(\mathbf{k})$ and $\omega''(\mathbf{k}) \neq 0$,

$$\xi(\mathbf{x},t) \approx a(\mathbf{x},t) \exp \{i\chi(\mathbf{x},t)\} , \quad (4)$$

where the phase function $\chi(\mathbf{x},t)$ has the form

$$\chi(\mathbf{x},t) = \mathbf{k}_s(\mathbf{x},t) \cdot \mathbf{x} - \omega(\mathbf{k}_s)t . \quad (5)$$

Note that Eq. 4 has the form of a plane wave but with amplitude, wave number, and frequency that are slowly varying functions of $\mathbf{x}$ and t.

By analogy with the plane wave case, we may define the local wave number and frequency associated with Eq. 4 as

$$\mathbf{k} = \nabla\chi \quad (6a)$$

and

$$\omega = -\frac{\partial\chi}{\partial t} . \quad (6b)$$

These equations imply that

$$\frac{\partial\mathbf{k}}{\partial t} + \nabla\omega = 0 , \quad (7)$$

which is known as the conservation of wave crests. This kinematic condition states that when no local sources are present, the rate of change of the wave number is balanced by the flux of wave crests past a given point; thus, crests are conserved. If we write the dispersion relation as

$$\omega = \omega_0 [\mathbf{k}(\mathbf{x},t), \lambda(\mathbf{x},t)] , \quad (8)$$

where the additional space-time dependence specified by $\lambda(\mathbf{x},t)$ allows for nonuniformity in the medium, Eq. 7 may be written as

$$\frac{\partial k_i}{\partial t} + \frac{\partial\omega_0}{\partial k_j} \frac{\partial k_j}{\partial x_i} + \frac{\partial\omega_0}{\partial \lambda} \frac{\partial \lambda}{\partial x_i} = 0 \quad (9a)$$

(where repeated indices are summed). We now notice from Eq. 3 that the point of stationary phase propagates with a velocity $\mathbf{C_g}$ given by

$$C_{gi} = \frac{\partial\omega_0}{\partial k_i} , \quad (9b)$$

which is known as the group velocity and, in fact, determines the spatial position at which Eq. 4 is valid for a particular $\mathbf{k}_s$. Using the group velocity and the fact that $\nabla \times \mathbf{k} = 0$ (see Eq. 6a), we may rewrite Eq. 9a as

$$\frac{\partial k_i}{\partial t} + C_{gj} \frac{\partial k_i}{\partial x_j} = -\frac{\partial \omega_0}{\partial \lambda} \frac{\partial \lambda}{\partial x_i} , \quad (10a)$$

and, by differentiating Eq. 8 with respect to time, we obtain

$$\frac{\partial \omega}{\partial t} + C_{gj} \frac{\partial \omega}{\partial x_j} = \frac{\partial \omega_0}{\partial \lambda} \frac{\partial \lambda}{\partial t} . \quad (10b)$$

Note that along the spatial curves defined by

$$\frac{dx_j}{dt} = C_{gj} , \quad (11)$$

the left-hand sides of Eqs. 10 may be written as total time derivatives. These curves are called rays, and from Eqs. 10 one can see that for a homogeneous, time-independent medium (λ = constant), $\mathbf{k}$ and ω are constant along a ray.

For waves propagating in a moving medium for which the current velocity $\mathbf{U}(\mathbf{x},t)$ varies over scales that are large compared to the wavelengths and periods of the waves, the frequency measured by a stationary observer is Doppler shifted to

$$\omega = \omega_0 + \mathbf{k} \cdot \mathbf{U} , \quad (12)$$

and the point of stationary phase now propagates along the curve defined by

$$\frac{dx_j}{dt} = C_{gj} + U_j . \quad (13)$$

Equations 10 then take the form

$$\frac{\partial k_i}{\partial t} + (C_{gj} + U_j) \frac{\partial k_i}{\partial x_j} = -\frac{\partial \omega_0}{\partial \lambda} \frac{\partial \lambda}{\partial x_i} - k_j \frac{\partial U_j}{\partial x_i}$$

$$(14a)$$

and

$$\frac{\partial \omega}{\partial t} + (C_{gj} + U_j) \frac{\partial \omega}{\partial x_j} = \frac{\partial \omega_0}{\partial \lambda} \frac{\partial \lambda}{\partial t} + k_j \frac{\partial U_j}{\partial t} . $$

$$(14b)$$

Note that as in the no-current case, Eqs. 14 may be written as total time derivatives along the rays defined by Eq. 13. For the case of a uniform medium (λ = constant) with a slowly varying current $\mathbf{U}(\mathbf{x},t)$, the kinematic conditions on $\mathbf{k}$ and ω (within the context of the stationary-phase approximation) are determined by the known dispersion relation (e.g., Eq. 8) and the coupled system of equations

$$\frac{dx_i}{dt} = \frac{\partial \omega_0}{\partial k_i} + U_i \quad (15a)$$

and

$$\frac{dk_i}{dt} = -k_j \frac{\partial U_j}{\partial x_i} . \quad (15b)$$

Equations 15 define ray trajectories or characteristics in four-dimensional phase space; it will be shown in the following paragraphs that the nature of the trajectories determines how energy is transported over the fluid surface.

We turn our attention now to the dynamical conditions that govern energy propagation. Let $\mathcal{E}(\mathbf{x},t)$ be the average energy density in the wave field described by Eq. 4 (averaged over time and space scales $O(1/\omega)$ and $O(1/k)$). Then the total wave energy between points x_1 and x_2 is given by

$$E(t) = \int_{x_1}^{x_2} \mathcal{E} \, dx , \quad (16)$$

where we consider the one-dimensional case for simplicity. Ray trajectories with associated group velocities C_{g1} and C_{g2} may be found that pass through x_1 and x_2, respectively. Then, since $x_1 = C_{g1}t$ and $x_2 = C_{g2}t$, we may write

$$\frac{dE}{dt} = \int_{x_1}^{x_2} \frac{\partial \mathcal{E}}{\partial t} \, dx + C_{g2}\mathcal{E}_2 - C_{g1}\mathcal{E}_1$$

$$= \int_{x_1}^{x_2} \left[\frac{\partial \mathcal{E}}{\partial t} + \frac{\partial}{\partial x} (C_g \mathcal{E}) \right] dx . \quad (17)$$

For a uniform medium with no current, the wave energy is conserved, i.e., $dE/dt = 0$, and we may write

$$\frac{\partial \mathcal{E}}{\partial t} + \nabla \cdot (\mathbf{C_g} \mathcal{E}) = 0 , \quad (18)$$

where we have reverted back to vector notation. From this equation we see that the energy is transported at the group velocity. Also, for a uniform medium with no currents, $\nabla \cdot \mathbf{C_g} = 0$, and the energy density remains constant along a ray trajectory.

Equation 18 may be generalized to the case of a nonuniform medium—in particular, to the case where a slowly varying current $\mathbf{U}(\mathbf{x},t)$ is present. This is most easily accomplished using variational methods,[3,4] and, in fact, leads to a new conservation equation for the quantity $\mathcal{E}/\omega_0$, called the wave action, of the form

$$\frac{\partial}{\partial t} \left(\frac{\mathcal{E}}{\omega_0} \right) + \nabla \cdot \left[(\mathbf{C_g} + \mathbf{U}) \frac{\mathcal{E}}{\omega_0} \right] = 0 . \quad (19)$$

In this equation, ω_0 is the intrinsic frequency in a local rest frame and $\mathbf{C_g} = \nabla_k \omega_0$. Equation 19 holds

for waves propagating in a medium whose properties are slowly varying compared to the waves, when no sources or sinks of energy are present. By separating out the ω_o variations, we may rewrite it (assuming a uniform medium, $\lambda = 0$) as an energy balance equation of the form

$$\frac{\partial \mathcal{E}}{\partial t} + \nabla \cdot [(\mathbf{C_g} + \mathbf{U})\mathcal{E}] = -\frac{\mathcal{E}}{\omega_0} \mathbf{k} \cdot (\mathbf{C_g} \cdot \nabla) \mathbf{U} . \tag{20}$$

Comparing Eq. 20 with Eq. 18, we see that when a surface current field $\mathbf{U}$ is present, the surface waves interact with the current via the term on the right side of Eq. 20. It is this term that generates the wave/current interaction. Note that when $\mathbf{U}$ is constant, there is no interaction and Eq. 20 takes the form of Eq. 18 with $\mathcal{E}$ transported along the ray trajectories with velocity $\mathbf{C_g} + \mathbf{U}$.

The result given by Eq. 19 may be modified to describe a general wave field by writing the wave action in terms of its spectral decomposition. If we define the action spectral density $N(\mathbf{k};\mathbf{x},t)$ by

$$A = \int N(\mathbf{k};\mathbf{x},t) \, d\mathbf{k} , \tag{21}$$

where A is the total action, it can be shown (see e.g., Ref. 5) that when no sources or sinks of energy are present,

$$\frac{dN}{dt} = \frac{\partial N}{\partial t} + (\mathbf{C_g} + \mathbf{U}) \cdot \nabla N = 0 , \tag{22}$$

where $N(\mathbf{k};\mathbf{x},t)$ may vary slowly in space and time because of the presence of the current field $\mathbf{U}$. Equation 22 states that (when no sources or sinks are present) the action spectral density N is constant along a ray trajectory, even when a surface current field is present. Note that this is not true, in general, for the total action A, which obeys Eq. 19. Equation 22 expresses conservation of wave action.

The total wave action A is related to the surface-wave-height power spectral density $S(\mathbf{k};\mathbf{x},t)$ by

$$A(\mathbf{x},t) = \rho g \int \frac{[1 + (k/k_m)^2]}{\omega_0(k)} S(\mathbf{k};\mathbf{x},t) \, d\mathbf{k} , \tag{23}$$

where the $(k/k_m)^2$ term is due to the effects of surface tension and ω_0 is given by the gravity-capillary dispersion relation

$$\omega_0^2 = gk[1 + (k/k_m)^2] . \tag{24}$$

In these equations, g is the acceleration of gravity; the fluid density, ρ, is assumed to be constant; and $k_m = 363$ radians per meter. From our previous defi-

nition of the action spectral density in Eq. 21, we obtain

$$N(\mathbf{k};\mathbf{x},t) = \rho \, \frac{\omega_0}{|\mathbf{k}|} \, S(\mathbf{k};\mathbf{x},t) , \tag{25}$$

which relates the action spectrum to the wave-height power spectrum. Thus, the conservation of action equation also describes the behavior of the surface-wave spectrum. In particular, when no currents are present, $\mathbf{k}$ (and hence ω_0) is constant and, therefore, according to Eq. 22, so is the power spectrum. When currents are present, the waves and current interact, and the surface-wave power spectrum is modified by the current field.

Up to this point, we have neglected sources or sinks of wave energy in our discussion. We know, however, that when a constant wind begins to blow on the smooth sea surface, surface waves develop—short waves at first, then longer and longer—until an equilibrium wave-height spectrum is reached and no further wave growth occurs. The equilibrium occurs when the energy input is balanced by dissipation effects. If the equilibrium is disturbed, for example, by a local surface current, the wind-dependent source/sink term will tend to force the spectrum back toward equilibrium. Therefore, in order to generalize the conservation of action as developed above, a source/sink term is required in order to account for the wind effects. The form of this term is a topic of current research and remains controversial (see e.g., Refs. 5, 7, and 8 and the references cited therein). In the present study, we adopt the source term described by Hughes[8] and recast Eq. 22 as an action balance equation in the form

$$\frac{dN(\mathbf{k};\mathbf{x},t)}{dt} = \beta(\mathbf{k})N(\mathbf{k};\mathbf{x},t) \left[1 - \frac{N(\mathbf{k};\mathbf{x},t)}{N_{eq}(\mathbf{k})} \right] , \tag{26}$$

where the time dependence of $\mathbf{k}$ and $\mathbf{x}$ is given by Eqs. 15, and $N_{eq}(\mathbf{k})$ represents the equilibrium (no-current) action spectrum that is independent of space and time. Note that the source/sink term on the right side of Eq. 26 is zero when $N = N_{eq}$ and positive (source) or negative (sink) depending on whether N is less than or greater than N_{eq}, respectively. Consequently, the source/sink term always tends to force N toward its equilibrium value N_{eq}. The strength of the forcing is determined by the function $\beta(\mathbf{k})$, the so-called relaxation rate. Since shorter surface waves respond more quickly to changes in the wind, $\beta(\mathbf{k})$ is an increasing function of $|\mathbf{k}|$, and for fixed $\mathbf{k}$, $\beta(\mathbf{k})$ increases with wind speed. There is, however, considerable uncertainty as to its exact functional form (see e.g., Refs. 8 and 9).

With the time dependence of $\mathbf{k}$ and $\mathbf{x}$ given by Eqs. 15, Eq. 26 is a first-order nonlinear differential equation for N. For $N > 0$, we may use the transformation $Q = 1/N$ to write Eq. 26 in the form

$$\frac{dQ}{dt} + \beta Q = \beta Q_{eq} , \qquad (27)$$

where $Q_{eq} = 1/N_{eq}$. The solution to this equation may be written as

$$Q(\mathbf{k};\mathbf{x},t) = Q_{eq}(\mathbf{k}) + N_{eq}(\mathbf{k}) \int_{-\infty}^{t} k_j' \frac{\partial U_j}{\partial x_i'} \frac{\partial Q_{eq}}{\partial k_i'}$$

$$\cdot \exp \left\{ -\int_{t'}^{t} \beta(\mathbf{k}'') \, dt'' \right\} dt' , \qquad (28)$$

where the primes and double primes on the $\mathbf{k}$ and $\mathbf{x}$ vectors correspond to the primes and double primes on the corresponding integration variables. Note that for $\beta(\mathbf{k}) = 0$, Eq. 28 yields the conservation of action result $Q[\mathbf{k}(t);\mathbf{x}(t),t] = Q_{eq}[k(-\infty)]$ as it should. We may now use this equation to determine the change in wave-height spectral density relative to the equilibrium value. In particular, using Eq. 25 to relate S to N (and our transformation $Q = 1/N$), we obtain

$$\frac{S(\mathbf{k};\mathbf{x},t)}{S_{eq}(\mathbf{k})} = [1 + P(\mathbf{k};\mathbf{x},t)]^{-1} , \qquad (29a)$$

where

$$P(\mathbf{k};\mathbf{x},t) = N_{eq}(\mathbf{k}) \int_{-\infty}^{t} k_j' \frac{\partial U_j}{\partial x_i'} \frac{\partial Q_{eq}}{\partial k_i'}$$

$$\cdot \exp \left\{ -\int_{-t'}^{t} \beta(\mathbf{k}'') \, dt'' \right\} dt' . \qquad (29b)$$

Equations 29 enable us to express the perturbation of the surface-wave-height spectrum for a particular $\mathbf{k}$ value at a specified spatial location as a function of the local surface current field, a specified equilibrium spectrum, and the relaxation rate $\beta(\mathbf{k})$.

In the following section, we discuss the results of our attempts to predict the intensity modulations observed in the SAR images of Fig. 1 using the wave/current interaction theory discussed above, with the measured internal-wave surface currents as input. In obtaining the results, we assume that the equilibrium wave-height spectrum $S_{eq}(\mathbf{k})$ is given by the modified Pierson spectrum described in Ref. 10, with a $\cos^4[(\theta_k - \theta_w)/2]$ angular dependence, where θ_k and θ_w specify the $\mathbf{k}$ and wind directions, respectively. This empirical spectrum provides a reasonable representation of spectral measurements over a wide range of $|\mathbf{k}|$ including the gravity-capillary and the capillary ranges. For the $\mathbf{k}$ values of interest in our study, the spectrum falls roughly like k^{-4}. Also, we have chosen for the relaxation rate $\beta(\mathbf{k})$, the parameterization given by Hughes.[8] The k dependence of $\beta(\mathbf{k})$ is shown in Fig. 2 for wind speeds (V_w) of 3 and 6 meters per
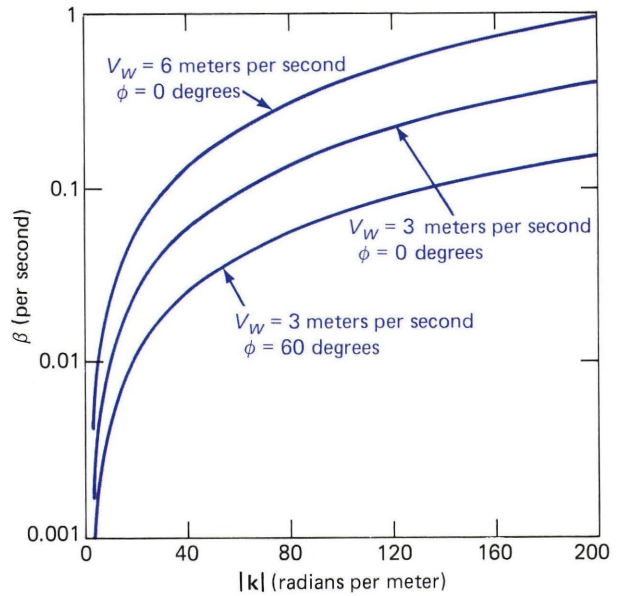

Figure 2—k-dependence of the surface-wave relaxation rate, β. The β curves are for wind speeds, V_w, of 3 and 6 meters per second and wind directions, ϕ, with respect to $\mathbf{k}$ of 0 and 60 degrees. The parameterization of $\beta(\mathbf{k})$ is that of Hughes.[8]

second blowing along the direction ϕ of 0 degrees, and 3 meters per second for $\phi = 60$ degrees. Note that for all cases shown, $\beta(\mathbf{k})$ increases relatively slowly for $k \gtrsim 60$ radians per meter but begins to decrease rapidly for $k \lesssim 60$ radians per meter.

INTENSITY MODULATION IN SAR IMAGES OF INTERNAL WAVES

Figure 1 shows L- and X-band SAR images of the surface manifestation of internal waves propagating toward the top (range direction) of the image. Each image spans about 5 kilometers in azimuth and about 6 kilometers in range, with the spacing between the four brightest waves at the top of the scene measuring about 0.5 to 1.5 kilometers. The SAR incidence angles to these waves range from around 25 to 47 degrees, which corresponds to Bragg wave numbers, k_B (equal to twice the projection of the radar wave number on the horizontal surface), of about 22 to 38 radians per meter for L band and about 166 to 287 radians per meter for X band. The research vessel USNS *Bartlett* can be seen clearly near the bottom center of each image, and the smaller vessel R/V *Cape* is the dim point seen most easily in the X-band image to the right and below *Bartlett*. The vessels collected ground-truth data by traversing the waves on parallel tracks toward the top of the scene about 15 minutes after the images shown in Fig. 1 were taken. The wind velocity was relatively constant at 6 meters per second toward an angle of 145 degrees with respect to the internal wave propagation direction (toward the top of the scene). One can easily see bright and dark streaks associated with each of the large waves in the L-band image but only bright streaks for the X-band case.

The relative modulation in the SAR intensity along the track of *Bartlett* is shown for X band in the upper plot of Fig. 3 and for L band in the lower plot. Both curves were obtained by averaging the SAR intensity over about 140 meters in the horizontal direction (azimuth), smoothing over about 30 meters along track (range), and normalizing so that the background intensity is unity. The peaks labeled waves 1 through 4 on the plots correspond to the first through fourth waves from the top of the appropriate image in Fig. 1. One can see from Fig. 3 that the enhancement in reflectivity (modulation greater than 1) for these four waves is nearly the same at L and X bands, while only the L-band return shows a definite region of reduced reflectivity (modulation less than 1) associated with each wave. Also, note that the position of the maximum modulation for each wave occurs at roughly the same distance from the ship at both L and X bands. An acceptable theory of the SAR imaging mechanism should account for each of these observations.

For the radar frequencies and incidence angles such as those in SARSEX, the radar backscatter from the ocean surface is given by the small perturbation or Bragg scattering limit,[11,12] where the radar cross section is proportional to the sum of the surface-wave-displacement power spectral densities $S(\mathbf{k},\mathbf{x})$ at the Bragg wave numbers $\pm\mathbf{k}_B$. Thus, for range-traveling waves such as those shown in Fig. 1, the SAR intensity modulation $M(\mathbf{k}_B,\mathbf{x})$ (or relative intensity) is given by

$$M(\mathbf{k}_B,\mathbf{x}) = \frac{S(\mathbf{k}_B,\mathbf{x}) + S(-\mathbf{k}_B,\mathbf{x})}{S_{eq}(\mathbf{k}_B) + S_{eq}(-\mathbf{k}_B)} , \qquad (30)$$

where both M and S are functions of position due to the presence of the surface-current field as discussed above.

We now use the measured surface currents and winds from SARSEX as inputs to the model described previously and compare the calculated intensity modulation with that measured from the SAR image. The surface currents were determined by using shipboard echo-sounder measurements of the internal-wave amplitude and towed-chain measurements of the thermocline displacement in conjunction with internal-wave theory[13] to construct analytic representations for the surface current associated with the waves. These currents were found to agree with direct measurements from the shipboard current meters and can be represented by the function $U_0 \operatorname{sech}^2 [K(x - C_I t)]$. Typical values for the current U_0 and peak current gradients for the waves shown in Fig. 1 are about 0.3 to 0.6 meter per second and 0.002 to 0.008 inverse second, respectively.

In Fig. 4, we show a comparison of the measured L-band intensity modulation over waves 2, 3, and 4, as described earlier, with the predictions from the wave/current interaction model. The model results shown by the colored curve in the upper plot in Fig. 4 were obtained using the analytic representation for the internal-wave surface currents, while those in the lower plot were computed directly from the ship-measured currents. In both cases, we have used the measured wind velocity (6 meters per second at ϕ = 145 degrees relative to the internal-wave propagation direction), Hughes relaxation rate,[8] and the modified Pierson equilibrium height spectrum[10] discussed previously. For the wind velocity and Bragg $\mathbf{k}$ values of interest here, only waves with $\mathbf{k} = -\mathbf{k}_B$ contribute significantly to Eq. 30. One can see from Fig.
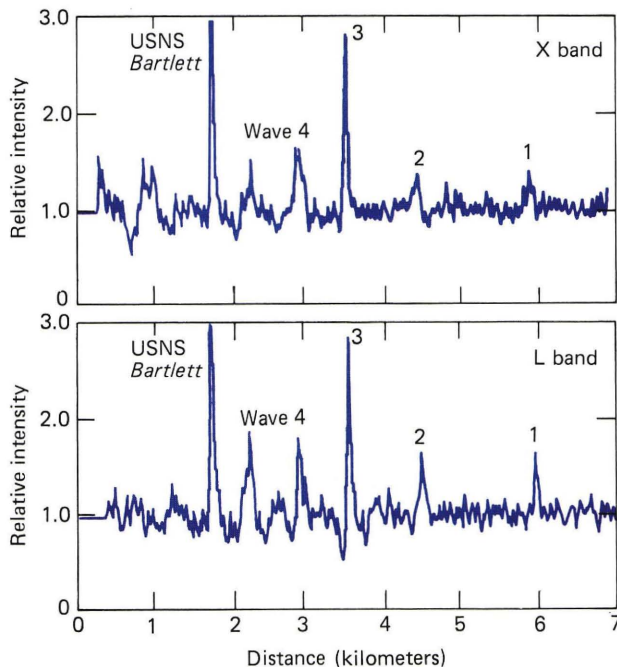

Figure 3—Relative intensity traces along the *Bartlett* track. Note that the large signal from *Bartlett* has been clipped at a relative intensity of 3.
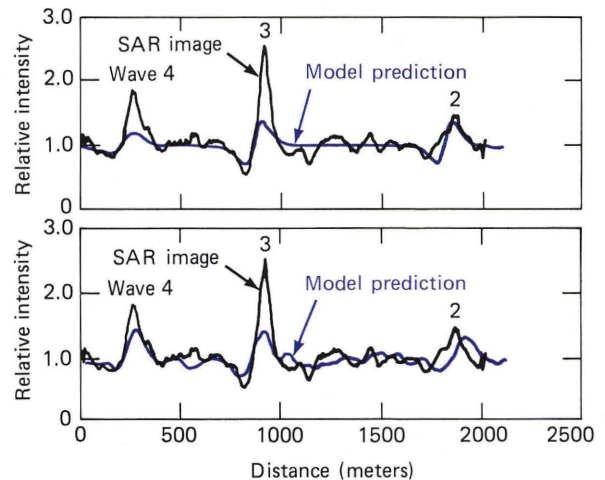

Figure 4—Comparison of the measured (black curves) and computed (colored curves) relative L-band intensity modulation for waves 2 through 4. The colored curve in the upper plot shows the calculated results obtained using an analytic representation of the internal-wave surface current in the vicinity of each wave. The colored curve in the lower plot shows the calculated results using the currents measured by the shipboard current meter.

4 that although the calculation somewhat underestimates the measured L-band modulation, the general agreement is quite encouraging. Note in particular that the calculated modulation reproduces the enhancement and reduction with nearly the same spatial variation as was observed in the measured data. We have also found that the computed modulation is roughly proportional to the horizontal current gradient, in agreement with the theory of Alpers.[14] Thus, within the experimental uncertainties in the exact value of the relaxation rates, we feel that the wave/current interaction theory outlined above can adequately explain the L-band SAR imaging of internal waves.

The situation at X band is not as clear. Application of the theory to compute the modulation of the X-band Bragg waves ($\lambda \approx 3$ centimeters) for the internal waves in Fig. 1 yields peak modulations of only a few percent of the background intensity as opposed to 20 to 50 percent at L band. Qualitatively, this occurs because the shorter X-band waves respond much more quickly to the wind than do the L-band waves. Thus, the relaxation rate in the X-band region is significantly larger and the source term in Eq. 26 is more effective in forcing the spectrum toward equilibrium than at L band. However, the measured X-band data, as shown by the upper plot in Fig. 3, show enhancements in the SAR intensity of the same order as those observed at L band and little reduction in intensity. These observations seem to indicate that although the presence of the internal-wave surface current does indeed produce enhanced roughening of the surface at X-band scales, the roughening is not due to direct modulation of X-band Bragg waves as described by Eq. 26. It is well known, however, that as gravity waves steepen to near the breaking point, they begin to lose energy by generating patches of small-scale roughness and by wave breaking.[5] We are therefore led to the hypothesis that the observed X-band modulation results from a two-step process in which increased small-scale roughening is generated as a result of the perturbation of the dominant wind waves by the internal-wave surface-current field.

In order to substantiate our hypothesis, we have computed the perturbation of the longer wavelength components of the surface spectrum by the measured internal-wave currents. Results for the internal wave 3 (as named above) surface current are presented in Fig. 5 for wavelengths ranging from 0.21 (L band) to 2π meters; the family of curves between $\lambda = 2\pi$ and $\lambda = 0.2\pi$ corresponds to wave numbers between 1 and 10 radians per meter in steps of 1 radian per meter. The propagation direction for each wave number was taken to be opposite the internal-wave propagation direction at an angle of 35 degrees with the wind (i.e., along $-\mathbf{k}_B$ as for the L-band wave). One can see from the plot that the position of maximum perturbation for the longer waves is near the peak of the internal-wave surface current (shown in the upper plot of Fig. 5). As the wavelength decreases, the position of this maximum shifts toward the position of the maximum (negative) gradient (shown in the middle plot in Fig.
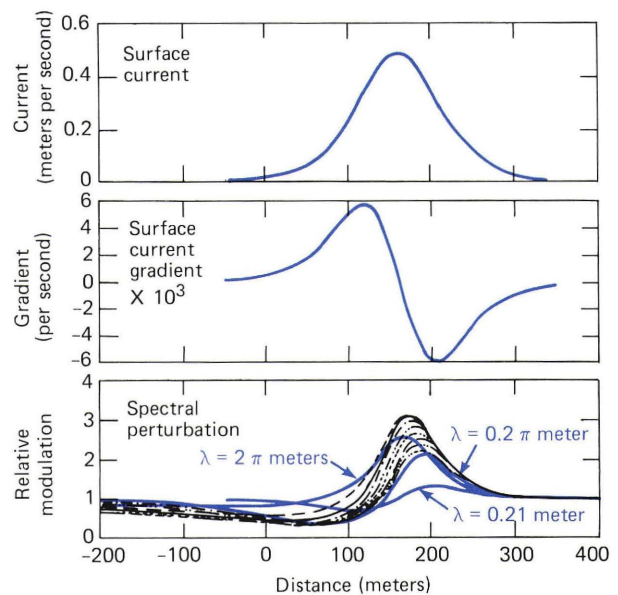

Figure 5—Comparison of the spatial behavior of the current and current gradient determined for wave 3 with that of the computed spectral modulation at several different wavelengths.

5). There are, moreover, peak modulations of between two and three times the equilibrium value throughout this entire region of the internal-wave phase. Although we cannot yet estimate quantitatively the degree to which the surface roughness is affected by the modulation of the longer meter-scale waves, it seems likely that it is large enough to cause a significant increase, for example, in the density of parasitic capillary waves or small-scale locally breaking waves to account for the observed increase in the X-band SAR return. The region of large modulation occurs between the peak internal-wave current and the peak (negative) current gradient, roughly the same location as for the maximum L-band perturbation. This is consistent with the observation from the data that the maximum L- and X-band modulation occurs at roughly the same position. In fact, the modulation of the longer waves should also produce additional L-band scatterers, perhaps explaining the slight underprediction of the maxima in the L-band SAR signatures discussed earlier. Finally, we see from Fig. 5 that there is an extended region where the meter-scale waves show a modulation less than unity. In that region, there should be no additional production of small-scale roughness via the two-step process discussed above, and the magnitude of the X-band Bragg components should therefore be comparable to their equilibrium value, thereby explaining why no noticeable dark bands, such as those observed at L band, are visible on the X-band images.

CONCLUSION

We have presented a brief discussion of the process by which surface waves are affected by the presence of local surface currents. In particular, we have developed a wave/current interaction model that can be

used to predict the modulation of the surface-wave-height spectrum as a function of position in a variable current field. With the assumption of Bragg scattering, the modulation evaluated at the Bragg wave number should be proportional to the intensity modulation in a SAR image of the current feature.

These ideas have been tested by using ground-truth measurements from SARSEX as inputs to the wave/current interaction model in order to compute the modulation of the surface-wave spectrum. With the assumption of Bragg scattering, the modulation at the Bragg wave number is proportional to the SAR intensity modulation. We have found, using the relaxation rate $\beta(\mathbf{k})$ of Hughes, that the predicted modulation at L band shows good overall agreement with measured data, although the magnitude of the predicted modulation is generally lower. Also, we have found that the predicted L-band modulation is roughly equal to $-4.5 \cap \partial U/\partial x[1/\beta(\mathbf{k}_B)]$. This means that the L-band modulation measurements and a knowledge of the horizontal current gradient could, in principle, be used to determine $\beta(\mathbf{k}_B)$. Alternatively, knowledge of the L-band modulation and $\beta(\mathbf{k}_B)$ could be used to determine the current gradient.

The measured SAR modulation at X band showed regions of enhanced intensity of the same order and at nearly the same positions as those observed at L-band, an enhancement that was almost an order of magnitude larger than that predicted by direct application of the wave/current interaction model to the X-band Bragg waves. However, the model predicts that the dominant wind waves show a maximum enhanced modulation two or three times the background level at roughly the same position in the internal-wave phase as the L-band peak. This finding has led to the speculation that the X-band modulation is directly connected to the small-scale roughness produced as a result of the modulation by the internal-wave current of the longer (more than a meter) wind waves, rather than by direct modulation of the X-band Bragg waves. We hope to strengthen this speculation by further analysis of additional SAR imagery under different environmental and imaging conditions where the character of these longer wave modulations can be quite different. The results of these analyses should add significantly to our growing understanding of the physics that governs SAR imaging of ocean surface currents.

REFERENCES

[1] R. C. Beal, P. S. DeLeonibus, and I. Katz, eds., *Spaceborne Synthetic Aperture Radar for Oceanography*, The Johns Hopkins University Press, Baltimore and London (1981).
[2] M. S. Longuet-Higgins and R. W. Stewart, "The Changes in Amplitude of Short Gravity Waves on Steady Nonuniform Currents," *J. Fluid Mech.* **10**, 529 (1961).
[3] F. P. Bretherton and C. J. R. Garrett, "Wavetrains in Inhomogeneous Moving Media," in *Proc. R. Soc. London* **S302**, p. 529 (1969).
[4] G. B. Whitham, *Linear and Nonlinear Waves*, John Wiley and Sons, New York (1974).
[5] O. M. Phillips, *The Dynamics of the Upper Ocean*, Cambridge University Press, New York (1977).
[6] P. H. LeBlond and L. A. Mysak, *Waves in the Ocean*, Elsevier Scientific Publishing Co., New York (1978).
[7] K. Hasselmann, "Weak Interaction Theory of Ocean Waves," in *Basic Development in Fluid Dynamics*, M. Hold, ed., Academic Press, New York (1968).
[8] B. A. Hughes, "The Effect of Internal Waves on Surface Wind Waves, Theoretical Analysis," *J. Geophys. Res.* **83C**, 455 (1978).
[9] W. J. Plant, "A Relationship between Wind Stress and Wave Slope," *J. Geophys. Res.* **87**, 1961-1967 (1982).
[10] A. W. Bjerkaas and F. W. Riedel, *Proposed Model for the Elevation Spectrum of a Wind-Roughened Sea Surface*, JHU/APL TG 1328 (1979).
[11] G. R. Valenzuela, "Scattering of Electromagnetic Waves from a Tilted Slightly Rough Surface," *Radio Sci.* **3**, 1057-1066 (1968).
[12] J. W. Wright, "A New Model for Sea Clutter," *IEEE Trans. Antennas Propag.* **AP-14**, 749-754 (1966).
[13] J. R. Apel and F. I. Gonzales, "Nonlinear Features of Internal Waves off Baja California as Observed from the Seasat Imaging Radar," *J. Geophys. Res.* **88**, 4459-4466 (1983).
[14] W. Alpers, "Theory of Radar Imaging of Internal Waves," *Nature* **314**, 245-247 (1985).

THE AUTHOR

DONALD R. THOMPSON was born in Sidney, Ohio, in 1942. He received a B.S. in physics from Case Western Reserve University in 1964 and a Ph.D. in physics from the University of Minnesota in 1968, where his thesis dealt with the quantum-mechanical description of few-nucleon scattering problems. After two years at the California Institute of Technology where he applied these methods to the study of reactions that govern stellar nucleosynthesis, Dr. Thompson returned to the University of Minnesota in 1970. In 1976, he was awarded an Alexander von Humboldt Foundation docent fellowship, which he used to continue his work on nuclear scattering theory at the Institute for Theoretical Physics at the University of Tübingen in West Germany. Dr. Thompson came to APL in 1980, where he has been working on the physics of ocean surface waves and remote sensing in the Systems Group of the Submarine Technology Department. He has published extensively and is a member of Tau Beta Pi, the American Physical Society, the American Association for the Advancement of Science, and the New York Academy of Sciences.